BIOLOGICAL SCIENCES

CLATHRIN LIGHT CHAIN DIVERSITY REGULATES MEMBRANE DEFORMATION IN VITRO AND SYNAPTIC VESICLE FORMATION IN VIVO

Lisa Redlingshöfer[1, 2], Faye McLeod[3, +], Yu Chen[1, 2], Marine D. Camus[1, 2], Jemima J. Burden[4], Ernest Palomer[3], Kit Briant[1, 2], Philip N. Dannhauser[1, 2, +], Patricia C. Salinas[3] and Frances M. Brodsky[1, 2]*

[1] Research Department of Structural and Molecular Biology, Division of Biosciences, University College London, Gower Street, London WC1E 6BT, UK

[2] Institute of Structural and Molecular Biology, Birkbeck and University College London, Malet Street, London WC1E 7HX, UK

[3] Research Department of Cell and Developmental Biology, Division of Biosciences, University College London, Gower Street, London WC1E 6BT, UK

[4] Medical Research Council Laboratory for Molecular Cell Biology, University College London, Gower Street, London WC1E 6BT, UK

* to whom correspondence should be addressed:
Professor Frances M. Brodsky
f.brodsky@ucl.ac.uk

[+] present addresses:
Dr Faye McLeod: Faculty of Medical Sciences, Newcastle University, Newcastle upon Tyne, NE2 4HH, United Kingdom

Dr Philip Dannhauser: Miltenyi Biotec B.V. & Co. KG, Friedrich-Ebert-Str. 68, 51429 Bergisch Gladbach, Germany

ABSTRACT

Clathrin light chain (CLC) subunits in vertebrates are encoded by paralogous genes *CLTA* and *CLTB* and both gene products are alternatively spliced in neurons. To understand how this CLC diversity influences neuronal clathrin function, we characterised the biophysical properties of clathrin comprising individual CLC variants for correlation with neuronal phenotypes of mice lacking either CLC-encoding gene. CLC splice variants differentially influenced clathrin knee conformation within assemblies, and clathrin with neuronal CLC mixtures was more effective in membrane deformation than clathrin with single neuronal isoforms nCLCa or nCLCb. Correspondingly, electrophysiological recordings revealed that neurons from mice lacking nCLCa or nCLCb were both defective in synaptic vesicle replenishment. Mice with only nCLCb had a reduced synaptic vesicle pool and impaired neurotransmission compared to wild-type mice, while nCLCa-only mice had increased synaptic vesicle numbers, restoring normal neurotransmission. These findings highlight differences between the CLC isoforms and show that isoform mixing influences tissue-specific clathrin activity in neurons, which requires their functional balance.

KEY WORDS

Clathrin, membrane traffic, coated vesicle formation, protein isoforms, neuronal synapse

SIGNIFICANCE STATEMENT

This study reveals that diversity of clathrin light chain (CLC) subunits alters clathrin properties and demonstrates that the two neuronal CLC subunits work together for optimal clathrin function in synaptic vesicle formation. Our findings establish a role for CLC diversity in synaptic transmission and illustrate how CLC variability expands the complexity of clathrin to serve tissue-specific functions.

INTRODUCTION

Clathrin mediates vesicle formation from the plasma membrane and endosomal compartments (1). Recruited by cargo-recognising adaptor proteins, triskelion-shaped clathrin proteins assemble into polyhedral lattices to capture membrane-associated cargo and promote membrane bending into clathrin-coated vesicles (CCVs). Through sequestration of a variety of cargo, CCVs play fundamental roles in general cellular physiology including regulation of nutrient uptake and signalling, as well as in tissue-specific membrane traffic such as synaptic vesicle (SV) generation (2). This range of clathrin functions has been attributed to adaptor and accessory protein variation (3). However, functional diversity is also generated by variability of clathrin subunits. Vertebrates have two types of clathrin heavy chains with distinct functions (4). The major vertebrate clathrin is formed from clathrin heavy chain CHC17 (herein referred to as CHC) associated with clathrin light chains (CLCs), which do not bind the minor CHC22 clathrin isoform. Vertebrate CLCs are encoded by two different genes *CLTA* and *CLTB* (in humans), producing CLCa and CLCb isoforms of about 60% sequence identity (5, 6). Their sequence differences have been conserved during evolution, after the encoding genes arose through duplication, suggesting the two isoforms can mediate distinct functions (7, 8). Expression levels of the CLCa and CLCb isoforms are tissue-specific (9), and further variation is created by alternative gene splicing during development (10) and in brain (5, 6). Here we address how CLC diversity affects the biophysical properties of clathrin and how the resulting variation affects the specialised function of clathrin in synaptic vesicle (SV) replenishment.

Limited functional differences between CLCa and CLCb have been observed in cell culture with respect to clathrin dynamics (11), during focal adhesion formation (12), cancer cell migration (13) and in epithelial polarity (14), with mechanisms attributed to isoform-specific differences in CLC binding proteins and post-translational modification (15). Loss of CLCs in

83 culture and *in vivo* affects CCV uptake of some, but not all cargo, possibly reflecting
84 variability in mechanical demand for packaging different cargo into CCVs (9, 15, 16). The
85 capacity for biophysical differences in clathrin comprising different CLC isoforms and their
86 splicing variants to influence tissue-specific clathrin functions has not yet been considered.
87 CLC variability has potential to affect clathrin function as CLCs interact with key domains of
88 the clathrin triskelion that contribute to clathrin-mediated membrane bending. They bind the
89 trimerisation domain (TxD) of the triskelion vertex where the three component CHCs interact
90 (17, 18), and extend along the triskelion leg to the bend at the knee where CLCs regulate
91 conformation (19). Like various other endocytic proteins (3), CLCs undergo neuron-specific
92 splicing (20), which introduces one exon in CLCb (encoding 18 residues) and two exons
93 (encoding 30 residues) in CLCa at equivalent positions near the CLC C-termini, resulting in
94 higher molecular weight forms nCLCb and nCLCa (5, 6), suggesting neuron-specific
95 functions for these variants. *In vitro*, CLCs are required for efficient clathrin-mediated
96 membrane vesiculation at low temperature (21). Thus, CLCs could affect clathrin-mediated
97 membrane deformation directly through their influence on clathrin lattice properties (21, 22),
98 as well as indirectly through cellular interaction with proteins that influence the actin
99 cytoskeleton (14, 23-25).
100
101 SV replenishment by membrane traffic following neuronal degranulation is critical for
102 sustained neurotransmission. Endocytosis is required to regulate synaptic plasma membrane
103 surface area and to retrieve SV proteins (26), and SVs are generated from the plasma
104 membrane and endosome-like compartments (27). The essential sites of clathrin function in
105 these pathways are debated (2, 28), but dysfunction of clathrin-associated endocytic proteins
106 is associated with neurological defects observed in Parkinson's disease (29), Alzheimer's
107 disease (3) and in numerous animal models in which such proteins have been genetically
108 deleted (30-35).
109

Here, we assess how clathrin lattices formed with neuronal and non-neuronal CLC variants could differentially affect function by correlating their *in vitro* biophysical properties with *in vivo* neuronal phenotypes of mice lacking CLC-encoding genes. We found that CLC composition significantly influenced clathrin lattice properties and the ability to form vesicles. CLC splice variation impacted assembly curvature by regulating CHC knee conformation, resulting in decreased ability of individual neuronal splice variants to deform liposome membrane *in vitro*. This effect was ameliorated for lattices formed from a mixture of neuronal CLC isoforms. Mice lacking either CLCa or CLCb isoforms showed corresponding differences in SV replenishment and synaptic neurotransmission compared to their wild-type (WT) littermates expressing both isoforms, and to each other. Collectively, these functional differences between CLC isoforms observed *in vitro* and *in vivo* establish a role for CLC diversity in regulating clathrin function in neurons and suggest a critical role for isoform balance.

RESULTS

CLC splice variants differentially influence lattice curvature via the triskelion knee

Within clathrin lattices, the knee bending angle determines whether a hexagon (non-curvature inducing) or pentagon (curvature-inducing) is formed (36, 37). In addition, the characteristic pucker at the triskelion vertex and the crossing angle of interacting CHC legs can further modulate lattice curvature (38, 39) (Fig. 1a). This versatility of clathrin assemblies allows clathrin to sequester cargo of various sizes as well as to form stable, flat assemblies that serve as signalling hubs (3, 40). For each closed cage, there is a fixed number of 12 pentagons, but a varying number of hexagons (41) (Fig. 1a). Thus, larger cages (i.e. lattices of lower curvature) have a smaller pentagon to hexagon ratio. CLCs maintain the puckered conformation of triskelia in flat assemblies (21) and structural studies showed that nCLCb can influence conformation of the triskelion knee up to a degree that inhibits assembly (19). Considering these effects on CHCs, we hypothesized that sequence differences between the CLC isoforms and alterations due to splicing might modulate CLC influence on triskelion conformation and lattice curvature.

To address this, we produced clathrin triskelia of defined CLC composition by reconstituting tissue-derived CHC triskelia (42) with recombinantly expressed CLCa, CLCb, nCLCa or nCLCb (SI Appendix, Fig. S1a-d). We then induced assembly of these different clathrins into closed cages and analysed cage diameter as a measure of lattice curvature by electron microscopy. Previous studies showed that tissue-derived, CLC-bound clathrin (native) forms two major size classes, while CHC-only triskelia predominantly form small-sized cages (43-46). Our results confirmed that without CLCs, CHC formed predominantly cages of less than 90 nm in diameter with an average size of around 70 nm, representing cages of up to 60 triskelia (45). Clathrin with each of the CLC variants was further able to form larger cages with an average diameter of around 110 nm (140 triskelia) for those cages. The degree to

151 which larger cages were formed varied significantly between splice variants (Fig. 1b, c),
152 indicating that the neuronal splice inserts regulate the influence of CLCs on lattice curvature.
153
154 To establish whether differences in larger cage formation resulted from CLC influence on the
155 triskelion vertex or on the CHC knee conformation or both, we dissected the effect of CLCs
156 separately for each domain. To test whether CLC diversity exerts influence through varying
157 CHC knee conformation, we produced clathrin cages from two CHC fragments that together
158 constitute a full-length clathrin triskelion “cut” at the knee (Fig. 1d) (47). The Hub fragment
159 (residues 1074-1675) was reconstituted with different CLCs (48) and combined with the
160 terminal-distal leg segment (TDD, residues 1-1074, SI Appendix, Fig. S1e) under conditions
161 promoting their co-assembly (47). Cages produced when TDD was combined with CLC-
162 reconstituted Hub fragments were similar in size to fragment cages without CLCs, and the
163 larger cages observed for CLC variants associated with intact CHC did not form (Fig. 1d, e).
164 This result demonstrates that for CLC diversity to exert an effect on lattice curvature, the
165 CHC knee must be intact, and shows that CLC splice variants differ in their influence on CHC
166 knee conformation. Formation of larger cages by neuronal CLCs suggests that the neuronal
167 splice inserts restrict the conformational flexibility of the CHC knee and could thereby reduce
168 the likelihood of pentagon over hexagon formation. Non-neuronal CLCs appear to support a
169 less biased variety of knee conformations, as cages of the two size classes are observed at
170 almost equal frequency (Fig. 1b, c). To establish whether cage size differences also
171 correlated with CLC effects at the TxD, the different CLCs were compared for their ability to
172 stabilise the TxD (SI Appendix, Fig. S2) in an assay that measures triskelion dissociation.
173 While dissociation differences were observed between triskelia reconstituted with the
174 different CLC isoforms and their splice variants, these effects did not correlate with cage size
175 differences, suggesting that CLC influence at the vertex is not a major factor in lattice
176 curvature.
177
178

CLC diversity modulates mechanical properties of the clathrin lattice

We next investigated whether the influence of CLCs on the CHC knee had mechanical consequences for their ability to support membrane deformation. Mechanical properties of clathrin lattices were previously shown to be CLC-dependent and reduced ability of CLC-free clathrin to bend membranes *in vitro* was correlated with reduced planar lattice quality when assembled on an electron microscopy (EM) grid (21). To establish whether CLC diversity influences lattice quality in the same assay, clathrins with different CLC composition were assembled on EM grids coated with a clathrin-binding fragment of epsin1 (H_6-ΔENTH-epsin$^{144-575}$, SI Appendix, Fig. S1f) (49). The flat lattices formed were visualized by EM and their periodicity (quality) assessed by Fourier transform analysis. Lattice quality was significantly reduced for clathrin with the neuronal splice variants of either CLCa or CLCb compared to clathrin reconstituted with their respective non-neuronal variants, and was significantly improved if formed from a 1:1 mix of nCLCa clathrin and nCLCb clathrin (Fig. 2). To visualise the nature of CLC distribution in these mixtures, lattices were generated using His-tagged nCLCa clathrin or nCLCb clathrin combined with the cognate untagged CLC and labelled with Ni-NTA-gold (SI Appendix, Fig. S3), confirming a uniform distribution of each neuronal CLC within the mixed lattice. In contrast to the behaviour of the neuronal CLCs, lattice quality was reduced in mixtures of CLCa clathrin and CLCb clathrin compared to lattices formed by clathrin with only CLCa or CLCb.

To determine whether CLC-related variation in lattice quality correlated with membrane bending efficacy, as seen for complete absence of CLCs, we tested the function of the CLC-reconstituted clathrins using a low temperature *in vitro* budding assay (21). In this assay, H_6-ΔENTH-epsin$^{144-575}$, coupled to liposomes via modified Ni-NTA lipids, captures clathrin at the liposome surface. Lattice assembly on these liposomes can generate mature buds, which remain attached to the liposome due to lack of dynamin, needed for scission (21, 49). The efficiency of clathrin with different CLC composition to form such coated buds was assessed at 15°C, a temperature permissive for budding by native clathrin but reduced for CLC-free

clathrin (21). For each reconstituted clathrin, we measured the diameter of clathrin-coated membrane profiles in thin-section electron micrographs and assessed budding efficiency by the percentage of mature clathrin-coated buds (defined by a fitted diameter < 200 nm) relative to the total clathrin-coated membrane observed including shallow pits and flat clathrin assemblies (defined by a fitted diameter > 200 nm) (Fig. 3a). In line with previous findings, we found that at 15°C native clathrin was about twice as effective in membrane deformation as CLC-free clathrin (21), and that budding efficiency varied with the CLC composition of clathrin tested (Fig. 3b). CLCa or CLCb clathrin lattices generated mature membrane buds more efficiently than clathrin with either single neuronal clathrin variant (Fig. 3b, c), demonstrating that CLC splicing affects budding. Visualising the clathrin-coated liposomes absorbed to EM grids confirmed that all clathrins tested assembled into intact lattices or buds on the liposome surface (SI Appendix, Fig. S4), suggesting that the observed variation in budding was not due to impaired lattice formation, but CLC-dependent lattice properties (21). Notably, mixing reconstituted neuronal clathrins significantly improved budding efficiency compared to clathrins with only one type of neuronal CLC (Fig. 3d), overall reflecting the same pattern as observed for both lattice quality and curvature (Table 1), suggesting all three parameters result from differential CLC effects at the triskelion knee. Furthermore, all three assays demonstrated that neuronal clathrin benefits from cooperative co-assembly of clathrin with both isoforms.

Membrane deformation could result either from lattice formation at constant curvature or through transitioning from flat to curved lattices (Fig. 3e). Morphological analyses of clathrin-coated pits in human cell lines suggest that clathrin initially assembles into flat lattices at the plasma membrane and then gradually deforms the underlying membrane into coated buds (50, 51). To determine whether clathrin displayed these budding characteristics in our *in vitro* system and whether they are influenced by CLCs, we adopted the same EM-based approach. In micrographs of clathrin buds formed on liposomes, we measured the angle between the convex side of the coat and the coat-free membrane (Fig. 3e), coat curvature

(i.e. diameter of the clathrin-coated structure), coat length and neck width for all coated membrane profiles (50) and then correlated these measurements. We observed a variety of coat curvatures (Fig. 3f) and found that neck width decreased with bud angle (Fig. 3g), as would be expected for both modes of deformation. Additionally, coat diameter correlated with the bud angle, characteristic of curvature transition (Fig. 3h), while we found no correlation between coat length and budding angle (Fig. 3i). Although this analysis is based on fixed structures at equilibrium, results were consistent with a flat to curved lattice transition, rather than assembly with constant curvature (Fig. 3h, i). Thus, we conclude that budding in our *in vitro* system displays the same characteristics as observed in cells (50, 51), where curvature is most likely generated gradually through lattice rearrangement. Collectively, our results suggest that CLC splice variants and mixtures thereof differ in their ability to promote this transition and that this is due to variable restrictive influence on the flexibility of the triskelion knee within the lattice, which in turn affects clathrin's mechanical ability to deform membrane into coated buds (Table 1).

CLC composition affects SV pool size and replenishment

Our *in vitro* experiments suggest that the CLCs differentially affect clathrin's ability to deform membrane, with the neuronal isoforms working in conjunction for efficient membrane budding. Therefore, we predicted that neurons of animals with only one CLC isoform might be defective in clathrin-mediated pathways that rely on SV formation. This hypothesis was investigated in knock-out (KO) mice lacking the *Clta* or *Cltb* genes in all tissues (CLCa KO and CLCb KO mice). We previously generated CLCa KO mice (9) and have now produced CLCb KO mice. Loss of *Cltb* in CLCb KO mice was confirmed by PCR, and no CLCb or nCLCb protein was detected in all tissues analysed (SI Appendix, Fig. S5). Whereas wild-type (WT) mice express a mixture of CLCs in most tissues (9), CLCa KO mice express only CLCb or nCLCb, and CLCb KO mice express only CLCa or nCLCa, enabling functional analysis of clathrin with only one type of CLC in neurons (Fig. 4a).

263 Hippocampal neurons have frequently been used to study the function of endocytic proteins
264 in synaptic transmission (27, 30, 31, 33, 34, 52). H&E staining of the hippocampus showed
265 no morphological abnormalities in either KO strain, indicating that absence of either CLC
266 isoform does not affect gross hippocampus development in the CLC KO mice (SI Appendix,
267 Fig. S6). We therefore analysed the adult hippocampus in the CLC KO and WT mice to
268 evaluate the function of mature excitatory synapses in the CA1 region, a region of well-
269 defined neuronal architecture and neurophysiological circuitry. For electrophysiological
270 recordings at Schaffer collateral (SC)-CA1 synapses in acute hippocampal slices, a
271 stimulating electrode was placed in the SC fibres of the CA3 region and responses were then
272 recorded in the CA1 pyramidal cell layer (Fig. 4b).
273
274 To determine the role of CLC diversity in SV pool replenishment *in vivo*, we recorded the
275 responses to a prolonged high-frequency stimulus, which maximally depletes presynaptic
276 terminals of the readily releasable pool (RRP) of SVs (53-55). Under these conditions, initial
277 responses would draw from the pre-existing SV pool, while sustained neurotransmission
278 would rely on the efficiency of SV pool replenishment (54). Using this approach, we were
279 able to assess CLC-dependency for different stages of SV exo- and endocytosis from these
280 recordings. We found that the initial fusion efficiency of SVs in either KO strain was similar to
281 that of their WT littermates, indicating that packaging of fusion-mediating cargo was not
282 affected by changes in CLC composition (Fig. 4c, d and SI Appendix, Fig. S7). Instead, both
283 KO models had a decreased SV recycling rate characteristic of a defect in acute SV pool
284 replenishment (Fig. 4c, d and SI Appendix, Fig. S7). This finding correlated with our
285 expectation from the *in vitro* studies that showed clathrin lattices with only one type of
286 neuronal CLC were different from mixed lattices in their assembly properties (Table 1).
287
288 Further calculations based on data obtained from sustained trains of action potentials
289 indicated that the RRP was larger in the CLCb KO mice but reduced in the CLCa KO mice
290 when compared to WT littermates (Fig. 4c, d and SI Appendix, Fig. S7), revealing a

phenotype that we did not expect from our *in vitro* data. To establish whether the SV formation was altered in the CLC KO mice rather than the ability to mobilise SVs from other SV pools, we assessed the ultrastructure of excitatory synapses in the CLC KO mice and their WT littermates (Fig. 4e). Indeed, SV density was significantly reduced in hippocampal neurons in the CLCa KO animals. In contrast, SV density in equivalent neurons of the CLCb KO mice was significantly increased compared to their WT littermates (Fig. 4f, j), in line with our RRP estimates from electrophysiological recordings (Fig. 4c, d). Other parameters such as individual SV size (Fig. 4g, k), postsynaptic density (PSD) length (Fig. 4h, l) and excitatory synapse density (Fig. 4i, m) were similar between both KO strains and respective WT littermates. Together, these data show that CLCs are required for efficient and sustained synaptic function and suggest that loss of either CLC decreases acute SV replenishment by affecting immediate formation, correlating with expectations from reduced in vitro budding efficiency, but that the KO strains differ in their ability to generally maintain SV pools. Thus, CLC composition influences SV density in excitatory neurons of the hippocampus, and nCLCa and nCLCb function differently in SV generation such that mice with only nCLCa can sustain a compensatory pathway for SV generation and mice with only nCLCb cannot.

CLCa KO and CLCb KO mice have distinct neurological and behavioural defects

To further investigate the differential consequences of CLCa or CLCb KO for synapse function, we conducted additional electrophysiological experiments to characterise synaptic transmission in our KO animals. Analyses of the evoked excitatory postsynaptic current (EPSC) responses to stimuli of increasing magnitude revealed decreased EPSC response amplitude in the CLCa KO mice compared to WT littermates, suggesting impaired basal synaptic transmission in the CLCa KO mice (Fig. 5a). In contrast, the evoked EPSC response amplitude in hippocampal slices from the CLCb KO mice was of similar or higher magnitude than that of their WT littermates, suggesting that basal synaptic transmission was intact and even enhanced (Fig. 5b). These differences in synaptic connectivity between hippocampal function in the two KO strains could arise from defects in presynaptic

neurotransmitter release correlating with differences in SV pool size in the KO animals relative to their WT littermates (Fig. 4).

We then performed paired-pulse ratio (PPR) recordings experiments, an approach that allows assessment of defects in neurotransmitter release (56, 57). In excitatory neurons such as those analysed here, a second stimulus pulse (P_2) fired in short succession after an initial pulse (P_1) results in a larger response than the first stimulus. This facilitation is dependent on changes in the probability of neurotransmitter release. PPR is inversely correlated with release probability, as a lower initial release probability leaves more vesicles remaining at the terminal which are then capable of being released after the second stimulus (56, 57). We observed that, compared to WT littermates, the PPR was increased in CLCa KO mice, consistent with a reduction in release probability (Fig. 5c). In contrast, no differences in PPR were observed in CLCb KO mice compared to WT littermates (Fig. 5d). Thus, specific loss of nCLCa impairs presynaptic function compromising neurotransmitter release at the SC-CA1 synapse. Collectively, our electrophysiological data support the morphological data (Fig. 4e-m), indicating that neurons with only nCLCa clathrin can compensate for defective SV regeneration by expanding their SV pool from another pathway, while neurons with only nCLCb clathrin cannot compensate and show decimated SV pools from impaired replenishment.

Ongoing breeding of the CLCa KO colony confirmed a 50% survival rate compared to that expected for homozygous CLCa KO mice (9), whereas homozygous CLCb KO mice had no survival defects (Fig. 5e). Survival phenotypes similar to the CLCa KO animals have been reported for other genetic deletions in endocytic pathways, which also displayed neuronal phenotypes (30) in the hippocampus and other regions of the brain (32). Therefore, we assessed performance in the rotarod test for neuro-motor coordination for both CLC KO mice (58). Compared to their WT littermates, surviving CLCa KO mice displayed defects in rotarod balance, whereas CLCb KO mice did not (Fig. 5f). Further assessment of sensorimotor

347 function revealed that CLCa KO mice exhibited defects in a grid-walking test (Fig. 5g), but
348 not in grip strength (Fig. 5h), suggesting neurological rather than muscular dysfunction in the
349 CLCa KO animals, supporting the notion that loss of nCLCa is less tolerable than loss of
350 nCLCb. Together, the phenotypes of the KO animals indicate that neuronal CLC isoforms are
351 differentially able to support compensatory mechanisms for adjusting SV pools hippocampal
352 synapses with impaired acute SV replenishment, and suggest that clathrin with only nCLCa
353 enables more functions than clathrin with only nCLCb, while a mix of both neuronal CLCs is
354 necessary for optimal clathrin function in neurons, in keeping with their synergistic
355 contribution to clathrin function *in vitro.*
356

DISCUSSION

To understand the consequences of CLC diversity for clathrin function, we characterised the biophysical properties of *in vitro* assemblies formed from clathrin comprising single CLC isoforms and correlated these properties with neuronal phenotypes observed in KO animals expressing single CLC isoforms. We found that neuronal CLC splicing affects lattice properties (Fig. 1b and Fig. 2b) by diversifying the CLC influence on the CHC knee to regulate lattice curvature (Fig. 1c, d) and deform membrane (Fig. 3b). Our *in vitro* studies further suggest that lattices formed from mixtures of clathrin with nCLCa and nCLCb have different assembly properties and are more efficient in membrane deformation compared to clathrin with only one type of neuronal CLC (Fig. 2b, 3d). Consistent with this observation, neurons from both CLCa and CLCb KO mice showed defects in synaptic transmission that indicated acute clathrin-dependent SV replenishment was impaired (Fig. 4c, d). However, the CLCa KO mice had reduced numbers of SVs in their hippocampal synapses, while the CLCb KO mice had more SVs than their WT littermates (Fig. 4f, j). Thus, although acute SV replenishment was impaired in both KO strains, clathrin with only nCLCa (in the CLCb KO mice) was able to support a compensatory pathway of SV formation, while clathrin with only nCLCb (in the CLCa KO) was not (Fig. 5a-d). These findings establish functional differences between CLC isoforms *in vitro* and *in vivo* and demonstrate how resulting clathrin diversity, as well as CLC isoform balance, are important for clathrin function in neurons.

Neuronal splicing predominates for CLCb in neurons (59), while neuronal CLCs are not present in other brain cells such as glial or Schwann cells (20), indicating that the CLC splice variants segregate within brain cell types to fulfil distinct functions. Neuronal CLC variation due to splicing had a significant influence on lattice curvature and budding efficiency. Compared to clathrin with non-neuronal CLCs, clathrin with neuronal CLCs formed predominantly large cages in solution (with low a pentagon to hexagon ratio), suggesting that through their influence on the CHC knee (Fig 1d), the spliced inserts reduce triskelion

385 flexibility to accommodate pentagonal faces. When constrained to a flat, solid surface (EM
386 grid), lattice assembly requires significant deformation of triskelia (21). The quality of lattices
387 formed by clathrin with neuronal CLCs under these conditions was reduced compared to
388 clathrin with non-neuronal CLCs, further suggesting that neuronal CLCs restrict clathrin's
389 conformational flexibility. Notably, CLC-dependent lattice quality and cage size correlated
390 with the ability of clathrin with different CLCs to produce mature buds at liposome
391 membranes, which morphological analysis suggested are generated by flat lattice
392 rearrangement, as observed at cell membranes (50, 51). Together, these results suggest
393 that CLC splicing variation influences clathrin's flexibility to form and alternate between a
394 range of morphologies in order to deform lipid membrane into mature clathrin-coated buds,
395 and that this is attributable to CLC influence on the CHC knee domain.
396
397 Given that the inserted sequences are located near the TxD where the C-termini of CLCs are
398 bound (arrowheads, Fig. 6a), we propose that the splice inserts affect the conformation of the
399 adjacent knee of a neighbouring triskelion, which is closer to the inserted sequences than the
400 knee of the triskelion to which the CLC is bound (Fig. 6b). This intermolecular influence could
401 involve splice inserts at the C-terminus (stars, Fig. 6b) interacting with the neighbouring CHC
402 knee or with the N-terminal domain (N) of a CLC bound to the neighbouring knee (Fig. 6b).
403 Considering the average 40% sequence differences between CLCa and CLCb isoforms and
404 their even greater variation at the N-terminus, inter-CLC interactions could vary depending
405 on which splice isoform interacts with which CLC isoform N-terminus, thereby influencing
406 overall lattice properties. This imputed interaction may be lost from clathrin with non-neuronal
407 CLCs, which would explain why mixing non-neuronal CLC isoforms does not affect *in vitro*
408 membrane deformation to the same extent as mixing neuronal CLC isoforms (Fig. 3d).
409
410 Here, we characterise the properties of homo- and hetero-assemblies of clathrin comprising
411 single CLC isoforms. In brain, CLC isoforms are apparently randomly distributed on triskelia
412 (60), in which case neuronal inserted sequences could still influence lattice curvature via

413 interactions with an adjacent triskelion knee. The presence of nCLCb would serve as an
414 attenuator of nCLCa-specific interactions and vice versa. Further, in cells where CLCb
415 expression is transiently increased (61), newly synthesized triskelia would be generally
416 occupied by a single CLC isoform as clathrin subunit turnover is slow (62). The resulting
417 homotypic clathrins would then participate mixed in lattices, as we have studied here. Thus,
418 neuronal CLC isoform expression ratios (and/or local abundance within cells) could tailor
419 clathrin lattice properties specifically to particular needs.
420
421 There are several pathways involved in SV recycling in neurons and the role of clathrin has
422 been widely debated, possibly because the contribution of each pathway to SV formation is
423 variable between organisms, types of neurons and stimulus (52, 63, 64). SV recycling can
424 either be achieved by direct regeneration of SVs through clathrin-mediated endocytosis from
425 the plasma membrane at low-frequency stimulus, or through clathrin-independent
426 mechanisms, which predominantly mediate retrieval of SV components from the plasma
427 membrane under high stimulus (2, 27, 28, 33, 52). Rapid clathrin-dependent trafficking of SV
428 proteins from the endosomal pathway then leads to re-sorting and formation of SVs at high-
429 frequency stimulus (2), which can occur in a timeframe of 1-3 seconds after stimulation (27).
430 In our analysis of neurotransmission, SV recycling defects were detected by
431 electrophysiology within three seconds at high stimulus (20 Hz for 3s), suggesting the
432 defects detected were due to impaired clathrin-mediated regeneration of SVs from the
433 endosomal pathway. These findings are consistent with previously observed roles for CLCs
434 in recycling from non-neuronal endosomal compartments (61, 65).
435
436 That neurons in both CLC KO strains shared an acute defect in SV pool replenishment fits
437 with our *in vitro* biophysical data that demonstrate single neuronal CLCs are not as efficient
438 in membrane deformation as a mixture of clathrin with both neuronal CLCs (Fig. 3d). In
439 response to this defect, we found that clathrin with only nCLCa generated an increased
440 steady-state SV pool in CLCb KO neurons, while clathrin with only nCLCb could not (Fig. 4).

441 CLCa seems to have preferential connection with the actin cytoskeleton compared to CLCb
442 (12, 14), which might account for the ability of nCLCa clathrin to function on its own without
443 nCLCb and benefit from involvement of actin and its accessory molecules in this
444 compensatory pathway. It is possible that in the (normal) presence of nCLCb, the actin
445 interactions of nCLCa may be “diluted down”, so that nCLCb works as an attenuating
446 balancing mechanism to control SV pools at steady state. The presence of nCLCb would
447 simultaneously create lattice properties for efficient CCV budding during neurotransmission.
448 In its absence, the acute replenishment pathway would decrease in efficiency but loss of the
449 nCLCb attenuation effect enables a compensatory pathway with nCLCa only (Fig. 6c). Thus,
450 the budding defect resulting from a change in biophysical properties of clathrin is detectable
451 only under acute demand, and when demand is less acute, there are mechanisms by which
452 nCLCa clathrin can generate SVs that are not supported by nCLCb clathrin.
453
454 Considering the whole animal phenotypes, including the increased mortality rate for CLCa
455 but not CLCb KO animals, CLCa seems able to sustain house-keeping clathrin functions,
456 while CLCb functions mainly in conjunction with CLCa, apparently in a regulatory capacity,
457 such that a balance between the two is required for some specialised functions. This is in line
458 with the observation that CLC expression ratios vary with tissue, and while lymphoid cells
459 almost exclusively express CLCa, no tissue has been found to express exclusively CLCb (9,
460 62). CLC isoform splicing changes during cell differentiation, development (10, 59) and ratios
461 of CLCb relative to CLCa are modulated in tumour progression (13) and cell migration (61).
462 These observations, in combination with the *in vitro* and *in vivo* data reported here, support
463 the concept that, in addition to influencing accessory protein interaction, the conserved CLC
464 isoform and splicing differences characteristic of vertebrates facilitate tissue-specific clathrin
465 functions by directly modulating clathrin lattice properties. In particular, CLC diversity
466 regulates clathrin budding efficiency, a property that we show here affects SV formation
467 under acute demand, and is likely to influence other pathways that rely on rapid clathrin-
468 mediated membrane traffic.

MATERIALS AND METHODS

Protein expression and purification

Except for full-length CHC, all proteins were recombinantly expressed in bacteria and purified by standard affinity and size exclusion chromatography methods as specified in SI Appendix, Materials and Methods. Native clathrin and full length CHC were prepared from porcine brain as specified in SI Appendix, Materials and Methods.

Characterisation of clathrin lattice properties

For lattice curvature determination, cage assembly was induced by dialysis in assembly-promoting buffer A (100 mM MES, 1 mM EGTA, 0.5 mM $MgCl_2$, 2 mM $CaCl_2$) and cage size distributions analysed form EM images as specified in SI Appendix, Materials and Methods. Flat lattices were produced and analysed as previously described (21) and as detailed in SI Appendix, Material and Methods. Lattice regularity was assessed from electron micrographs of similar quality and various focuses for each specimen as a measure of lattice quality. 5-12 images were analysed for each reconstituted clathrin isoform within each of three independent sets of experiments. *In vitro* budding was performed as previously described (49). In brief, H_6-ΔENTH-epsin$^{144-575}$ was bound to liposomes made from brain polar lipid extracts containing 5% DGS-Ni-NTA lipids (Avanti). H_6-ΔENTH-epsin$^{144-575}$-coated liposomes were then chilled to 15°C and mixed with clathrin triskelia at 15°C, incubated for 30 min at 15°C and then transferred to ice. Samples were then fixed at 4°C overnight and processed for EM analysis. Diameter, coat length, bud angle and neck width of clathrin-coated membrane profiles were measured from electron micrographs using ImageJ (NIH) and data processed using Prism (GraphPad). Between 150 and 200 coat profiles, randomly sampled across four thin sections, were analysed for each sample (> 60,000 nm total coat length per experiment per sample). The proportion of mature buds, defined by a diameter of less than 200 nm, of all clathrin-coated membrane profiles examined, was used as a measure of

budding efficiency. Results from 3-5 independent sets of experiments were tested for statistical significance.

Generation of CLC KO mice

The *Cltb*$^{ko/ko}$ mouse strain was created from ES cell clone 19159A-F4, generated by Regeneron Pharmaceuticals, Inc., and obtained from the KOMP Repository (www.komp.org). Methods used to create the CLCb-null ES cell clone have previously been published (66). In brief, the complete coding region of the *Cltb* gene was fully deleted by homologous recombination using a large BAC-based targeting vector. Targeted ES cells were then injected into albino C57BL/6J-N blastocytes and transferred into foster mothers. Chimeric offspring were mated with C57BL/6J females (Charles River), and germ-line transmission of the *Cltb*-null allele (*Cltb*^{ko}) was established. Heterozygote *Cltb*$^{ko/+}$ mice were backcrossed on the C57BL/6 background and bred to produce *Cltb*$^{ko/ko}$ homozygous mice. CLCa KO mice were derived from C57BL/6 WT mice (9) and produced by breeding *Clta*$^{ko/+}$ heterozygotes. WT littermates from the same breedings were used as controls for homozyogous KO animals. All procedures involving animals were conducted according to the Animals Scientific Procedures Act UK (1986) and in compliance with the ethical standards at University College London (UCL).

Analysis of protein expression in brain

Mouse brains were harvested from six 9-12-month old C57BL/6 WT and homozygous CLCa and CLCb KO mice and snap-frozen in liquid nitrogen and stored at −80°C until further use. Tissue were quickly thawed and homogenised in lysis buffer (50 mM HEPES pH 8.0, 50 mM NaCl, 1% Triton-X 100, 5 mM EDTA, 2 mM $CaCl_2$, 1 mM PMSF, cOmplete™ Protease Inhibitor Cocktail mix (Roche)). The homogenate was further incubated on ice for 45 min before centrifugation at 21,000 g and 4°C for 2 x 10 min in an Eppendorf 5424 R benchtop centrifuge (Eppendorf). Protein content of the lysate was determined by BCA assay (Thermo

Fisher). For analysis, 25 µg of sample was loaded on 4-15% acrylamide gels (Bio-Rad) and subjected to SDS-PAGE and immunoblotting. Primary antibodies used for immunoblotting were TD.1 (anti-CHC, made in house) (67), X16 (anti-CLCa, made in house) (68), CLTB (anti-CLCb, Proteintech) and anti-beta-actin (Sigma-Aldrich).

Electrophysiology

Experiments were performed in 8-10-month-old mice. Both male and female mice were used for electrophysiological experiments. Acute transverse hippocampal slices (300 µm) of homozygous CLCa or CLCb KO and control mice were cut on a Leica VT-1000 vibratome in ice-cold artificial cerebrospinal fluid (ACSF) bubbled with 95% O_2/5% CO_2 containing (in mM): NaCl (125), KCl (2.4), $NaHCO_3$ (26), NaH_2PO_4 (1.4), D-(+)-Glucose (20), $CaCl_2$ (0.5) and $MgCl_2$ (3). At 5-minute intervals, slices were then transferred into a series of 3 different chambers oxygenated (95% O_2/5% CO_2) in the same base ACSF but with the following temperature and component (in mM) variations: **1.** 21°C initially with $MgCl_2$ (1) and $CaCl_2$ (0.5) then allowed to heat gradually to 36°C; **2.** 36°C with $MgCl_2$ (1) and $CaCl_2$ (1); and **3**. 36°C initially with $MgCl_2$ (1) and $CaCl_2$ (2) before cooling to 21°C. Slices were then left for at least 1 hour before recordings commenced.

Evoked recordings were performed on an upright microscope continually perfused with oxygenated recording solution at room temperature containing the same ACSF composition as the third chamber and supplemented with 10 µM bicuculline. Pyramidal cells in the CA1 region were held at -60 mV in whole-cell voltage-clamp configuration using glass microelectrodes (resistance 3-8 MΩ) filled with caesium gluconate intracellular solution containing (in mM): D-gluconic acid lactone (130), HEPES (10), EGTA (10), NaCl (10), $CaCl_2$ (0.5), $MgCl_2$(1), ATP (1) and GTP (0.5), QX314 (5), pH to 7.2 with CsOH. To evoke postsynaptic EPSCs, a bipolar concentric stimulation electrode (FHC) was placed in the SC fibres of the CA3 region. For input-output recordings, the stimulus pulse was varied between 0.2 and 1 mA with a pulse width of 0.1 millisecond (ms) and stimuli were delivered at a rate

of 0.1 Hz. Paired pulse stimuli were given at rate of 0.2 Hz with different inter-stimulus intervals, ranging from 25 ms to 200 ms and a stimulation strength set to approximately 50% of the maximal response for each cell. PPR was calculated as the ratio of the peak amplitude of the second response over the first response. Calculation of RRP size, initial fusion efficiency and SV recycling rate was done on ESPC recordings that underwent 3 s duration trains of stimulation at 20Hz and estimated as previously described (54, 69). Briefly, RRP size, fusion efficiency (*fe*) and vesicle recycling rate (α) were evaluated from the cumulative charge during the stimulation train using the following two equations:

Equation 1:

$$fe = \frac{r(1)}{r(\infty)}(1 - \exp(-\alpha\Delta t))$$

Equation 2:

$$fe = \frac{r(1)}{\sum_{i=1}^{s} r(i)\exp(-\alpha(S-i)\Delta t)}$$

r(1) is the charge of the first EPSC in the train

r(i) the charge passed by the *i*th EPSC

r(∞) was calculated from the average charge of the last 10 EPSCs in the train

Δ*t* is the stimulus interval in the train

The RRP was estimated as RRP=*r*(1)/*fe*.

All currents were recorded using an Axopatch 200B amplifier, filtered (1 kHz) and digitised (10 kHz). Data were monitored online and analysed offline using WinEDR and WinWCP software (available free online at http://spider.science.strath.ac.uk/sipbs/software_ses.htm). Stimulus artefacts in representative traces were digitally removed for clarity.

Statistical analysis

All experiments were performed at least three times. All calculations and graphs were performed with ImageJ, Microsoft Excel and GraphPad Prism software. P-values were

579 calculated using two-tailed Student's unpaired or paired (*in vitro* budding) t-tests, two-way
580 ANOVA with repeated measures (electrophysiology), one-way ANOVA followed by Holm-
581 Sidak correction for multiple comparison or one-way ANOVA for preselected pairs without
582 correction for multiple comparison (clathrin biophysical properties). Detailed statistical
583 information including statistical tests used, number of independent experiments, P-values
584 and definition of error bars is described in individual figure legends.
585
586 **Additional methods**
587 Details on methods for protein purification and assays, mouse genotyping and behavioural
588 tests, electron microscopy and ultrastructure analysis are in SI Appendix, Materials and
589 Methods.
590
591 **Data availability**
592 Protein expression vectors, non-commercial antibodies and mouse strains produced in this
593 study are available upon request. All data generated and analysed for this study and
594 associated protocols are included in the main text or SI Appendix.

595 **ACKNOWLEDGMENTS**

596 This work was supported by grants to F. M. B. from the Wellcome Trust (107858/Z/15/Z), to
597 P.C.S. from the Medical Research Council (MR/M024083/1) and to P.C.S. and E. P. from
598 Alzheimer's Research UK (ARUK-PG2018A-002). L. R. was supported by a Wellcome Trust
599 4-year interdisciplinary PhD studentship. J. J. B. was supported by MRC funding to the MRC
600 Laboratory of Molecular Cell Biology at UCL, award code MC_U12266B. P. N. D. was
601 supported by a UCL Excellence Fellowship. The authors would like to acknowledge UCL
602 IQPath, UCL Institute of Neurology, Queen Square London, WC1N 3BG for processing
603 tissue slices for H&E staining and Massimo Signore (ICH) and Anna Crowley (KLB
604 Transgenic facility, UCL) for the generation of the *Cltb*^{ko} mouse strain.

605

606 **AUTHOR CONTRIBUTIONS**

607 The study was conceived by L. R. and F. M. B. with expert input from P. N. D., F. M., E. P.
608 and P. C. S. and the project was managed by F.M.B. Electrophysiology experiments were
609 conducted and analysed by F. M. All *in vitro* reconstitution, protein level and EM experiments
610 and analyses were carried out by L. R. with expert assistance from J. J. B., F. M., E. P., P. N.
611 D. and K. B. Mouse behaviour data and survival characteristics were collected by Y. C. and
612 M. D. C. The paper was written by L. R., F. M. B., F. M. and P. C. S. and then all authors
613 read and commented on the paper.

614

615 **COMPETING INTEREST**

616 The authors declare no competing interest.

617

REFERENCES

1. F. M. Brodsky, Diversity of clathrin function: new tricks for an old protein. *Annu Rev Cell Dev Biol* **28**, 309-336 (2012).

2. T. Soykan, T. Maritzen, V. Haucke, Modes and mechanisms of synaptic vesicle recycling. *Curr Opin Neurobiol* **39**, 17-23 (2016).

3. H. T. McMahon, E. Boucrot, Molecular mechanism and physiological functions of clathrin-mediated endocytosis. *Nat Rev Mol Cell Biol* **12**, 517-533 (2011).

4. P. N. Dannhauser *et al.*, CHC22 and CHC17 clathrins have distinct biochemical properties and display differential regulation and function. *J Biol Chem* **292**, 20834-20844 (2017).

5. A. P. Jackson, H. F. Seow, N. Holmes, K. Drickamer, P. Parham, Clathrin light chains contain brain-specific insertion sequences and a region of homology with intermediate filaments. *Nature* **326**, 154-159 (1987).

6. T. Kirchhausen *et al.*, Clathrin light chains LCA and LCB are similar, polymorphic, and share repeated heptad motifs. *Science* **236**, 320-324 (1987).

7. D. E. Wakeham *et al.*, Clathrin heavy and light chain isoforms originated by independent mechanisms of gene duplication during chordate evolution. *Proc Natl Acad Sci U S A* **102**, 7209-7214 (2005).

8. M. Fumagalli *et al.*, Genetic diversity of CHC22 clathrin impacts its function in glucose metabolism. *eLife* **8** (2019).

9. S. Wu *et al.*, Clathrin light chains' role in selective endocytosis influences antibody isotype switching. *Proc Natl Acad Sci U S A* **113**, 9816-9821 (2016).

10. J. Giudice *et al.*, Alternative splicing regulates vesicular trafficking genes in cardiomyocytes during postnatal heart development. *Nat Commun* **5**, 3603 (2014).

11. M. Mettlen *et al.*, Endocytic accessory proteins are functionally distinguished by their differential effects on the maturation of clathrin-coated pits. *Mol Biol Cell* **20**, 3251-3260 (2009).

12. O. M. Tsygankova, J. H. Keen, A unique role for clathrin light chain A in cell spreading and migration. *J Cell Sci* 10.1242/jcs.224030 (2019).

13. P. H. Chen *et al.*, Crosstalk between CLCb/Dyn1-mediated adaptive clathrin-mediated endocytosis and epidermal growth factor receptor signaling increases metastasis. *Dev Cell* **40**, 278-288.e275 (2017).

14. M. Biancospino *et al.*, Clathrin light chain A drives selective myosin VI recruitment to clathrin-coated pits under membrane tension. *Nat Commun* **10**, 4974 (2019).

15. H. Maib, F. Ferreira, S. Vassilopoulos, E. Smythe, Cargo regulates clathrin-coated pit invagination via clathrin light chain phosphorylation. *J Cell Biol* **217**, 4253 (2018).

16. J. C. Stachowiak, F. M. Brodsky, E. A. Miller, A cost-benefit analysis of the physical mechanisms of membrane curvature. *Nat Cell Biol* **15**, 1019-1027 (2013).

17. J. A. Ybe *et al.*, Light chain C-terminal region reinforces the stability of clathrin heavy chain trimers. *Traffic* **8**, 1101-1110 (2007).

18. D. S. Chu, B. Pishvaee, G. S. Payne, The light chain subunit is required for clathrin function in Saccharomyces cerevisiae. *J Biol Chem* **271**, 33123-33130 (1996).

19. J. D. Wilbur *et al.*, Conformation switching of clathrin light chain regulates clathrin lattice assembly. *Dev Cell* **18**, 841-848 (2010).

20. D. H. Wong *et al.*, Neuron-specific expression of high-molecular-weight clathrin light chain. *J Neurosci* **10**, 3025-3031 (1990).

21. P. N. Dannhauser *et al.*, Effect of clathrin light chains on the stiffness of clathrin lattices and membrane budding. *Traffic* **16**, 519-533 (2015).

22. M. Lherbette, L. Redlingshofer, F. M. Brodsky, I. A. T. Schaap, P. N. Dannhauser, The AP2 adaptor enhances clathrin coat stiffness. *FEBS J* **286**, 4074-4085 (2019).

23. C. Y. Chen, F. M. Brodsky, Huntingtin-interacting protein 1 (Hip1) and Hip1-related protein (Hip1R) bind the conserved sequence of clathrin light chains and thereby influence clathrin assembly in vitro and actin distribution in vivo. *J Biol Chem* **280**, 6109-6117 (2005).

24. J. D. Wilbur *et al.*, Actin binding by Hip1 (huntingtin-interacting protein 1) and Hip1R (Hip1-related protein) is regulated by clathrin light chain. *J Biol Chem* **283**, 32870-32879 (2008).

25. A. M. Schreij *et al.*, LRRK2 localizes to endosomes and interacts with clathrin-light chains to limit Rac1 activation. *EMBO Rep* **16**, 79-86 (2014).

26. J. E. Heuser, T. S. Reese, Evidence for recycling of synaptic vesicle membrane during transmitter release at the frog neuromuscular junction. *Journal of Cell Biology* **57**, 315-344 (1973).

27. S. Watanabe *et al.*, Clathrin regenerates synaptic vesicles from endosomes. *Nature* **515**, 228-233 (2014).

28. S. Watanabe, E. Boucrot, Fast and ultrafast endocytosis. *Curr Opin Cell Biol* **47**, 64-71 (2017).

29. S. F. Soukup, R. Vanhauwaert, P. Verstreken, Parkinson's disease: convergence on synaptic homeostasis. *EMBO J* **37**, e98960 (2018).

30. S. J. Koo *et al.*, Vesicular synaptobrevin/VAMP2 levels guarded by AP180 control efficient neurotransmission. *Neuron* **88**, 330-344 (2015).

31. M. Cao *et al.*, Parkinson Sac domain mutation in synaptojanin 1 impairs clathrin uncoating at synapses and triggers dystrophic changes in dopaminergic axons. *Neuron* **93**, 882-896.e885 (2017).

32. I. Milosevic *et al.*, Recruitment of endophilin to clathrin-coated pit necks is required for efficient vesicle uncoating after fission. *Neuron* **72**, 587-601 (2011).

33. N. L. Kononenko *et al.*, Clathrin/AP-2 mediate synaptic vesicle reformation from endosome-like vacuoles but are not essential for membrane retrieval at central synapses. *Neuron* **82**, 981-988 (2014).

34. Y.-I. Yim *et al.*, Endocytosis and clathrin-uncoating defects at synapses of auxilin knockout mice. *Proc Natl Acad Sci U S A* **107**, 4412 (2010).

35. T. Mitsunari *et al.*, Clathrin adaptor AP-2 is essential for early embryonal development. *Mol Cell Biol* **25**, 9318-9323 (2005).

36. A. Musacchio *et al.*, Functional organization of clathrin in coats: combining electron cryomicroscopy and X-ray crystallography. *Mol Cell* **3**, 761-770 (1999).

37. K. L. Morris *et al.*, Cryo-EM of multiple cage architectures reveals a universal mode of clathrin self-assembly. *Nat Struct Mol Biol* **26**, 890-898 (2019).

38. W. K. den Otter, M. R. Renes, W. J. Briels, Self-assembly of three-legged patchy particles into polyhedral cages. *J Phys: Condens Matter* **22**, 104103 (2010).

39. A. Fotin *et al.*, Molecular model for a complete clathrin lattice from electron cryomicroscopy. *Nature* **432**, 573-579 (2004).

40. F. Baschieri *et al.*, Frustrated endocytosis controls contractility-independent mechanotransduction at clathrin-coated structures. *Nat Commun* **9**, 3825 (2018).

41. S. Schein, Architecture of clathrin fullerene cages reflects a geometric constraint--the head-to-tail exclusion rule--and a preference for asymmetry. *J Mol Biol* **387**, 363-375 (2009).

42. F. K. Winkler, K. K. Stanley, Clathrin heavy chain, light chain interactions. *EMBO J* **2**, 1393-1400 (1983).

43. P. K. Nandi, H. T. Pretorius, R. E. Lippoldt, M. L. Johnson, H. Edelhoch, Molecular properties of the reassembled coat protein of coated vesicles. *Biochemistry* **19**, 5917-5921 (1980).

44. P. P. Van Jaarsveld, P. K. Nandi, R. E. Lippoldt, H. Saroff, H. Edelhoch, Polymerization of clathrin protomers into basket structures. *Biochemistry* **20**, 4129-4135 (1981).

45. J. Heuser, T. Kirchhausen, Deep-etch views of clathrin assemblies. *J Ultrastruct Res* **92**, 1-27 (1985).

46. E. Ungewickell, H. Ungewickell, Bovine brain clathrin light chains impede heavy chain assembly in vitro. *J Biol Chem* **266**, 12710-12714 (1991).

47. B. Greene, S. H. Liu, A. Wilde, F. M. Brodsky, Complete reconstitution of clathrin basket formation with recombinant protein fragments: adaptor control of clathrin self-assembly. *Traffic* **1**, 69-75 (2000).

48. S.-H. Liu, M. L. Wong, C. S. Craik, F. M. Brodsky, Regulation of clathrin assembly and trimerization defined using recombinant triskelion hubs. *Cell* **83**, 257-267 (1995).

49. P. N. Dannhauser, E. J. Ungewickell, Reconstitution of clathrin-coated bud and vesicle formation with minimal components. *Nat Cell Biol* **14**, 634-639 (2012).

50. O. Avinoam, M. Schorb, C. J. Beese, J. A. G. Briggs, M. Kaksonen, Endocytic sites mature by continuous bending and remodeling of the clathrin coat. *Science* **348**, 1369-1372 (2015).

51. B. L. Scott *et al.*, Membrane bending occurs at all stages of clathrin-coat assembly and defines endocytic dynamics. *Nat Commun* **9**, 419 (2018).

52. S. Watanabe *et al.*, Ultrafast endocytosis at mouse hippocampal synapses. *Nature* **504**, 242-247 (2013).

53. L. E. Dobrunz, Release probability is regulated by the size of the readily releasable vesicle pool at excitatory synapses in hippocampus. *Int J Dev Neurosci* **20**, 225-236 (2002).

54. J. F. Wesseling, D. C. Lo, Limit on the role of activity in controlling the release-ready supply of synaptic vesicles. *J Neurosci* **22**, 9708-9720 (2002).

55. C. F. Stevens, J. H. Williams, Discharge of the readily releasable pool with action potentials at hippocampal synapses. *J Neurophysiol* **98**, 3221-3229 (2007).

56. L. E. Dobrunz, C. F. Stevens, Heterogeneity of release probability, facilitation, and depletion at central synapses. *Neuron* **18**, 995-1008 (1997).

57. R. S. Zucker, W. G. Regehr, Short-term synaptic plasticity. *Annu Rev Physiol* **64**, 355-405 (2002).

58. H. Shiotsuki *et al.*, A rotarod test for evaluation of motor skill learning. *J Neurosci Methods* **189**, 180-185 (2010).

59. S. Stamm *et al.*, Clathrin light chain B: gene structure and neuron-specific splicing. *Nucleic Acids Res* **20**, 5097-5103 (1992).

60. T. Kirchhausen, S. C. Harrison, P. Parham, F. M. Brodsky, Location and distribution of the light chains in clathrin trimers. *Proc Natl Acad Sci U S A* **80**, 2481-2485 (1983).

61. S. R. Majeed *et al.*, Clathrin light chains are required for the gyrating-clathrin recycling pathway and thereby promote cell migration. *Nat Commun* **5**, 3891 (2014).

62. S. L. Acton, Brodsky, F. M., Predominance of clathrin light chain LCb correlates with the presence of a regulated secretory pathway. *J Cell Biol* **111**, 1419-1426 (1990).

63. H. Heerssen, R. D. Fetter, G. W. Davis, Clathrin dependence of synaptic-vesicle formation at the Drosophila neuromuscular junction. *Curr Biol* **18**, 401-409 (2008).

64. K. Sato *et al.*, Differential requirements for clathrin in receptor-mediated endocytosis and maintenance of synaptic vesicle pools. *Proc Natl Acad Sci U S A* **106**, 1139-1144 (2009).

65. V. Poupon *et al.*, Clathrin light chains function in mannose phosphate receptor trafficking via regulation of actin assembly. *Proc Natl Acad Sci U S A* **105**, 168-173 (2008).

66. D. M. Valenzuela *et al.*, High-throughput engineering of the mouse genome coupled with high-resolution expression analysis. *Nat Biotechnol* **21**, 652-659 (2003).

771 67. I. S. Näthke *et al.*, Folding and trimerization of clathrin subunits at the triskelion hub.
772 *Cell* **68**, 899-910 (1992).

773 68. F. M. Brodsky, Clathrin structure characterized with monoclonal antibodies. II.
774 Identification of in vivo forms of clathrin. *J Cell Biol* **101**, 2055-2062 (1985).

775 69. L. Ciani *et al.*, Wnt signalling tunes neurotransmitter release by directly targeting
776 Synaptotagmin-1. *Nat Commun* **6**, 8302 (2015).

777

TABLES

Table 1: Regulation of clathrin lattice properties by CLC isoforms

	high					low
Lattice curvature	CLCb	CLCa	nCLCa/b	CLCa/b	nCLCa	nCLCb
Lattice quality	CLCb	CLCa	nCLCa/b	CLCa/b	nCLCa	nCLCb
Budding efficiency	CLCb	CLCa	nCLCa/b	CLCa/b	nCLCa	nCLCb

FIGURE LEGENDS

Fig. 1: CLCs differentially affect lattice curvature via regulation at the CHC knee. **a** Pucker (1) and knee (2) angles of the clathrin triskelion (black: CHC, blue: CLC) dictate lattice architecture. Different knee angles (encircled, black straight and dashed lines) are adopted for hexagon (non-curvature inducing) or pentagon (curvature inducing) formation (3, whole triskelion in black and parts of others in grey). Lattice curvature is further amended through changes in pucker angle (4, dashed and black lines), or changes in proximal leg-crossing angle (5). CLC subunits are omitted for simplicity. Different sizes of closed cages are achieved by varying numbers of hexagons and a fixed number of 12 pentagons (filled black, based on (45)). **b** Quantification of the percentage of small cages (< 90 nm in diameter) in a population of more than 200 cages, generated by *in vitro* assembly of clathrin reconstituted with indicated CLCs, 1:1 mixtures of reconstituted clathrins (CLCa/b or nCLCa/b) or CHC only (CHC), determined from electron micrographs (mean ± SEM, **P* < 0.05, ****P* < 0.001 one-way ANOVA followed by Holm-Sidak correction for multiple comparison, n = 3). **c** Cage size distributions from assemblies of triskelia formed from full length CHC as described in **b**, with CLC composition key in d. **d** Size distributions of cages formed from TDD (black) and Hub (grey) co-assemblies, with Hub fragments reconstituted or not with the indicated CLC

802 isoforms or 1:1 mixtures thereof. **e** Representative EM images of cages formed from full-
803 length CHC (top) or Hub/TDD fragments (bottom) without or following reconstitution with
804 indicated CLC isoforms. Scale bar: 100 nm.
805
806 **Fig. 2**: CLC splicing and mixing affects *in vitro* lattice quality. **a** Clathrin reconstituted with
807 indicated CLC isoforms and mixtures thereof were assembled into flat lattices and visualised
808 by negative stain for EM analysis. Scale bar: 200 nm. **b** Quality (regularity quantified by
809 Fourier transform) of lattices generated as in **a**, (mean ± SEM, **P* < 0.05, ***P* < 0.01, one-
810 way ANOVA followed by Holm-Sidak correction for multiple comparison, n = 5). **c** Differences
811 in lattice quality between indicated reconstituted clathrins in individual experiments as in **b**
812 (data points and mean ± SEM, n = 5).
813
814 **Fig. 3**: CLC splicing and mixing affects *in vitro* lattice budding efficiency. **a** Representative
815 EM images of clathrin reconstituted with indicated CLC isoforms, 1:1 mixtures thereof, CHC
816 only (CHC) and tissue-derived clathrin (native) assemblies on H_6-ΔENTH-epsin$^{144-575}$-coated
817 liposomes. Scale bar: 200 nm. **b** Quantification of the percentage of mature buds (defined as
818 clathrin-coated membrane profiles with < 200 nm fitted diameter) of more than 60,000 nm
819 total clathrin-coated membrane profiles including flat, shallow and mature structures
820 generated as in **a** (mean ± SEM, **P* < 0.05, ***P* < 0.01, paired Student's t-test for native and
821 CHC, n = 3, one-way ANOVA with repeated measures for CLC-reconstituted clathrin, n = 4).
822 **c** Differences in percentage of mature buds between indicated reconstituted clathrins in
823 individual experiments in **b** (data points and mean ± SEM, n = 4). **d** Quantification of budding
824 efficiency (% mature buds determined as in **b**, normalised to native) of reconstituted clathrins
825 and mixtures thereof (**P* < 0.05, one-way ANOVA for sets of neuronal or non-neuronal
826 samples, followed by Holm-Sidak correction for multiple comparison, n = 3, p = 0.052,
827 Student's t-test for neuronal and non-neuronal mixtures, n = 3). **e** Parameters characterising
828 coated buds (top); coat length *c*, membrane bud diameter *d*, neck width *n*, and budding angle

829 θ. Models of clathrin-mediated membrane deformation by transitional curvature generation
830 and lattice rearrangement (middle) or lattice growth under constant lattice curvature (bottom).
831 **f** Representative coat profiles for flat (left), shallow (middle), and mature budded (< 200 nm
832 fitted diameter, right) structures. **g** to **i** Analysis of the dataset generated as shown in **a** for
833 coated membrane parameters *n* (**g**), *d* (**h**) and *c* (**i**) as shown in **e** in relation to the θ of each
834 structure measured for all reconstituted clathrins within the same experiment. Inserts in **h**
835 and **i** show the different correlations of these parameters as predicted according to the
836 curvature transition (red, straight line) and constant curvature models (red, dashed line)
837 shown in **e**.
838
839 **Fig. 4:** CLC composition regulates SV pool replenishment in hippocampal neurons. **a**
840 Immunoblot of CLC KO and WT brain lysate for CHC (TD.1 antibody), CLCa (X16 antibody),
841 CLCb (CLTB antibody) and actin (anti-beta-actin antibody). **b** Schematic illustration of
842 stimulating and recording electrode setup in acute hippocampal slices. The synapses
843 investigated are formed by a Schaffer-collateral (SC) axon (black) from a pyramidal neuron
844 (black triangles, cell bodies) in the CA3 region synapsing with a receiving pyramidal neuron
845 (grey triangle, cell body) in the CA1 region from which responses are recorded. Black circles
846 denote dentate gyrus (DG) granule cell bodies. **c** Representative traces of evoked excitatory
847 postsynaptic currents (EPSCs) following a 20 Hz electrical stimulation for 3 s in CLCa KO
848 and WT hippocampal slices (left). Graphs (right) show the mean (± SEM) initial fusion
849 efficiency, SV recycling rate and readily releasable pool (RRP) size calculated for all cells (n
850 = 9-11 cells from 3 animals/genotype; **P* < 0.05 and ***P* < 0.01, unpaired Student's t-test). **d**
851 Representative traces of EPSCs following a 20 Hz electrical stimulation for 3 s in CLCb KO
852 and WT hippocampus slices (left). Graphs (right) show the mean (± SEM) initial fusion
853 efficiency, SV recycling rate and RRP size calculated for all cells (n = 11-12 cells from 4
854 animals/genotype; **P* < 0.05, unpaired Student's t-test)**. e** Representative EM images of
855 excitatory synapses in the CA1 region of the hippocampus of CLCa WT, CLCa KO, CLCb

856 WT and CLCb KO. Scale bars; 300 nm. **f** to **m** Quantification of data extracted from EM
857 images as in **e**. Graphs show SV density within 300 nm of the PSD (**e** and **i**), cumulative
858 frequency distribution of SV size (**g** and **k**), postsynaptic density (PSD) length (**h** and **l**) and
859 synapse density (**i** and **m**) expressed as mean ± SEM (*P < 0.05, unpaired Student's t-test, n
860 = 3).
861
862 **Fig. 5**: Neuronal defects are compensated for in CLCb KO but not CLCa KO mice. **a** Input-
863 output relationship of evoked excitatory postsynaptic currents (EPSCs) at CA1 synapses of
864 WT and CLCa KO hippocampus slices. Traces show responses of representative cells at
865 increasing stimulus intensity with an average of 3 responses for each stimulus strength
866 (mean ± SEM; n = 9-11 cells from 3 animals/genotype; *P < 0.05, two-way ANOVA with
867 repeated measures). **b** Input-output relationship of evoked EPSCs at CA1 synapses of WT
868 and CLCb KO hippocampus slices. Traces show response of representative cells at
869 increasing stimulus intensity with an average of 3 responses for each stimulus strength
870 (mean ± SEM; n = 12-15 cells from 4 animals/genotype; *P < 0.05, two-way ANOVA with
871 repeated measures). **c** Paired-pulse ratio (PPR) of evoked EPSCs at CA1 synapses of WT
872 and CLCa KO hippocampal slices. Traces show responses of representative cells. Graph
873 displays the mean PPR (P_2/P_1 ± SEM) from all cells (n = 9-11 cells from 3 animals/genotype)
874 at different time intervals between paired pulses (***P < 0.001, unpaired Student's t-test). **d**
875 PPR of EPSCs at CA1 synapses of WT and CLCb KO hippocampal slices. Traces show
876 responses of representative cells. Graph displays the mean PPR (P_2/P_1 ± SEM) from all cells
877 (n = 12-15 cells from 4 animals/genotype) at different time intervals between paired pulses. **e**
878 Genotype distribution for CLCa KO (n = 590) and CLCb KO (n = 359) mice after weaning
879 compared to expected distribution (****P < 0.0001, *Chi*-square test). **f** Performance in the
880 accelerated rotarod test (latency to fall) by CLC KO (CLCa KO = 8, CLCb KO = 8) and
881 control wild-type littermates (CLCa WT = 8, CLCb WT = 7) expressed as data points and
882 mean ± SEM (****P < 0.0001, unpaired Student's t-test). **g** Time to cross grid for CLCa KO (n

883 = 10) and control mice (n = 10) expressed as data points and mean ± SEM (*P < 0.05,
884 unpaired Student's t-test). **h** Grip strength of CLCa KO (n = 10) and control mice (n = 11,
885 gram-force relative grip strength over body weight) expressed as data points and mean ±
886 SEM.
887
888 **Fig. 6:** Model of how neuronal CLC diversity regulates synaptic vesicle recycling and lattice
889 properties. **a** CLC (cyan) neuronal splice inserts (arrowheads) are located near the TxD of
890 the bound CHC (green, left, PDB: 3LVH). **b** CLC (cyan) neuronal splice inserts (stars) are
891 near the CHC knee of the neighbouring triskelion (red or orange) within lattices (right, PDB:
892 3IYV). Interaction between a neuronal splicing insert and the knee of an adjacent triskelion
893 and/or adjacent CLC N-terminus (N) could promote conformational change in the CHC knee.
894 As the formation of pentagons and hexagons requires different knee angles, this interaction
895 could consequently influence lattice curvature (see Fig. 1a). **c** In WT mice (centre), a mix of
896 nCLCa and nCLCb clathrin creates the appropriate biophysical properties to mediate SV
897 generation from endosomal compartments (and possibly the plasma membrane, blue-green
898 arrows). Loss of nCLCa (left) creates nCLCb clathrin lattices that are defective in efficient SV
899 regeneration (blue arrows), resulting in decimated SV pools. Loss of nCLCb (right) creates
900 nCLCa clathrin lattices, which are also less efficient in SV regeneration than WT, but able to
901 maintain an overall increased SV pool by excess budding to compensate for reduced
902 efficiency in acute SV pool replenishment (green arrows).

Figure 1

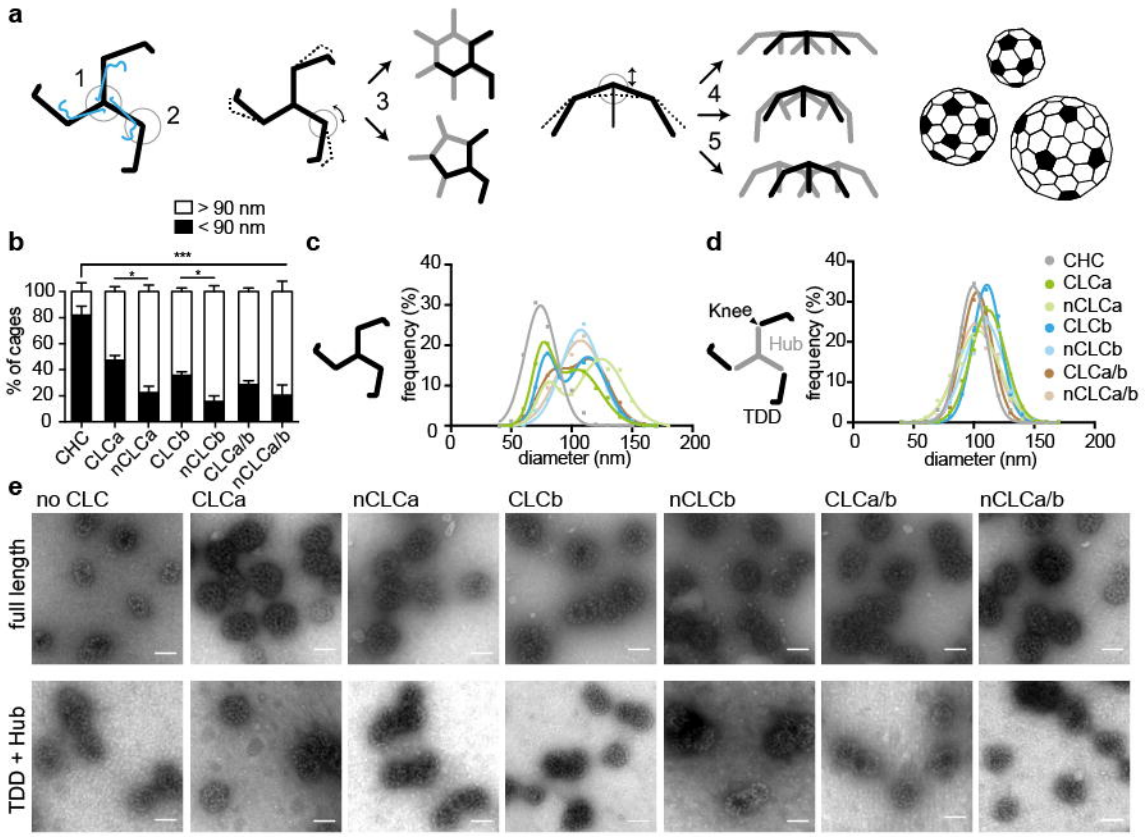
a
1
2
3
4
5
b
> 90 nm
< 90 nm
***
*
*
% of cages
100
80
60
40
20
0
CHC
CLCa
nCLCa
CLCb
nCLCb
CLCa/b
nCLCa/b
c
frequency (%)
40
30
20
10
0
0
50
100
150
200
diameter (nm)
d
Knee
Hub
TDD
frequency (%)
diameter (nm)
CHC
CLCa
nCLCa
CLCb
nCLCb
CLCa/b
nCLCa/b
e
no CLC
CLCa
nCLCa
CLCb
nCLCb
CLCa/b
nCLCa/b
full length
TDD + Hub

Figure 2

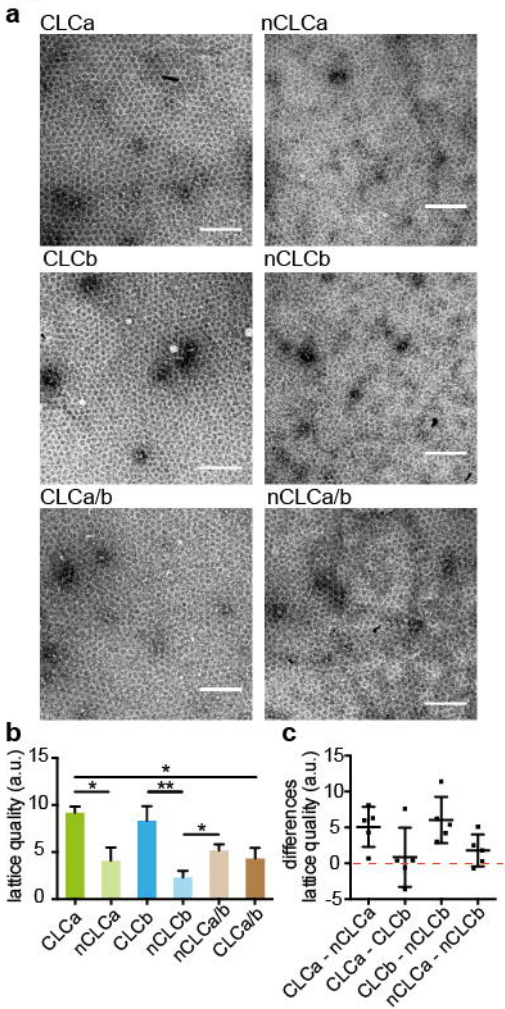
a
CLCa
nCLCa
CLCb
nCLCb
CLCa/b
nCLCa/b
b
lattice quality (a.u.)
15
10
5
0
*
*
**
*
CLCa
nCLCa
CLCb
nCLCb
nCLCa/b
CLCa/b
c
differences lattice quality (a.u.)
15
10
5
0
-5
CLCa - nCLCa
CLCa - CLCb
CLCb - nCLCb
nCLCa - nCLCb

Figure 3

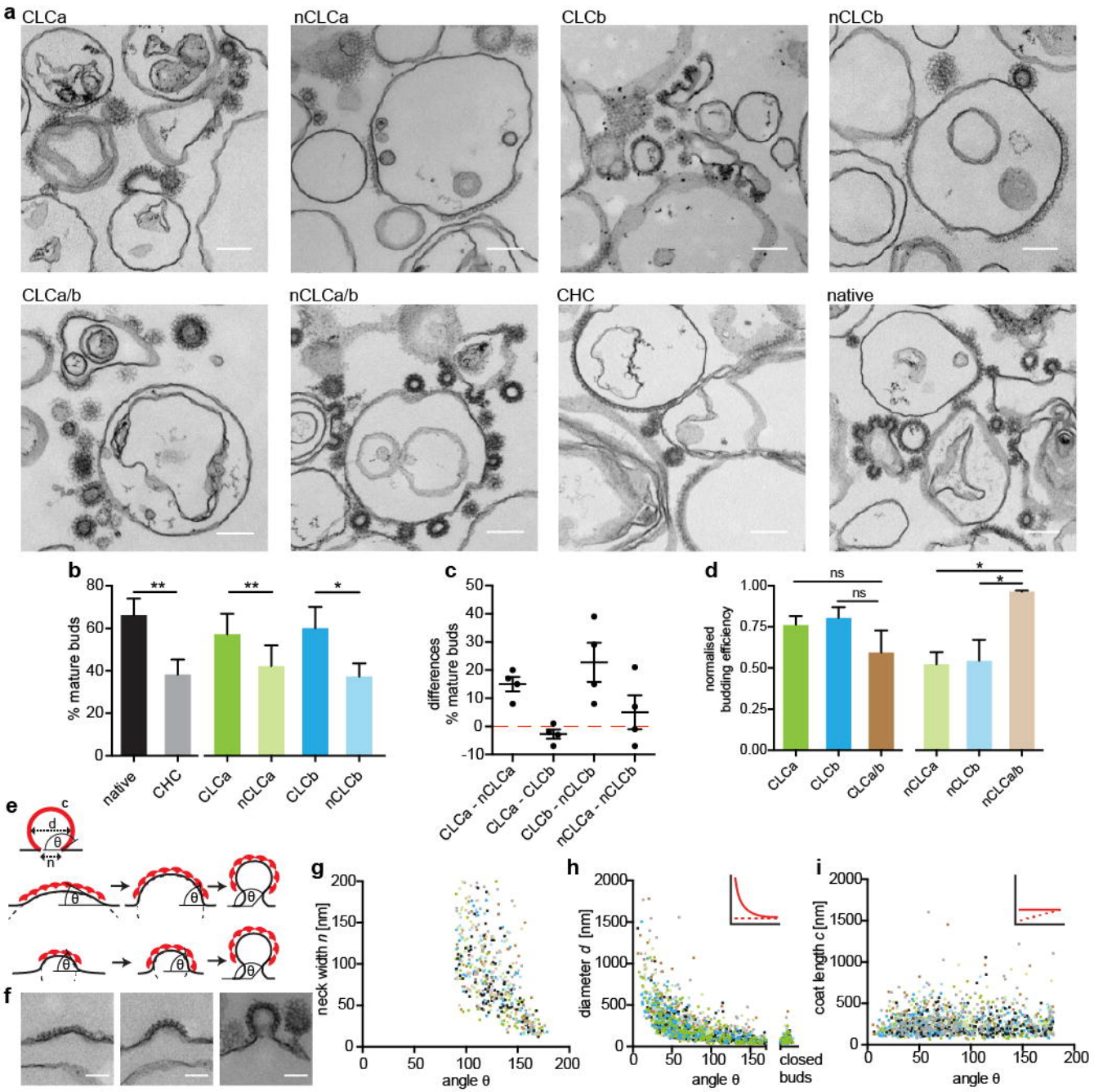
a
CLCa
nCLCa
CLCb
nCLCb
CLCa/b
nCLCa/b
CHC
native
b
% mature buds
native
CHC
CLCa
nCLCa
CLCb
nCLCb
c
differences % mature buds
CLCa - nCLCa
CLCa - CLCb
CLCb - nCLCb
nCLCa - nCLCb
d
normalised budding efficiency
ns
CLCa
CLCb
CLCa/b
nCLCa
nCLCb
nCLCa/b
e
f
g
neck width n [nm]
angle θ
h
diameter d [nm]
closed buds
i
coat length c [nm]

Figure 4

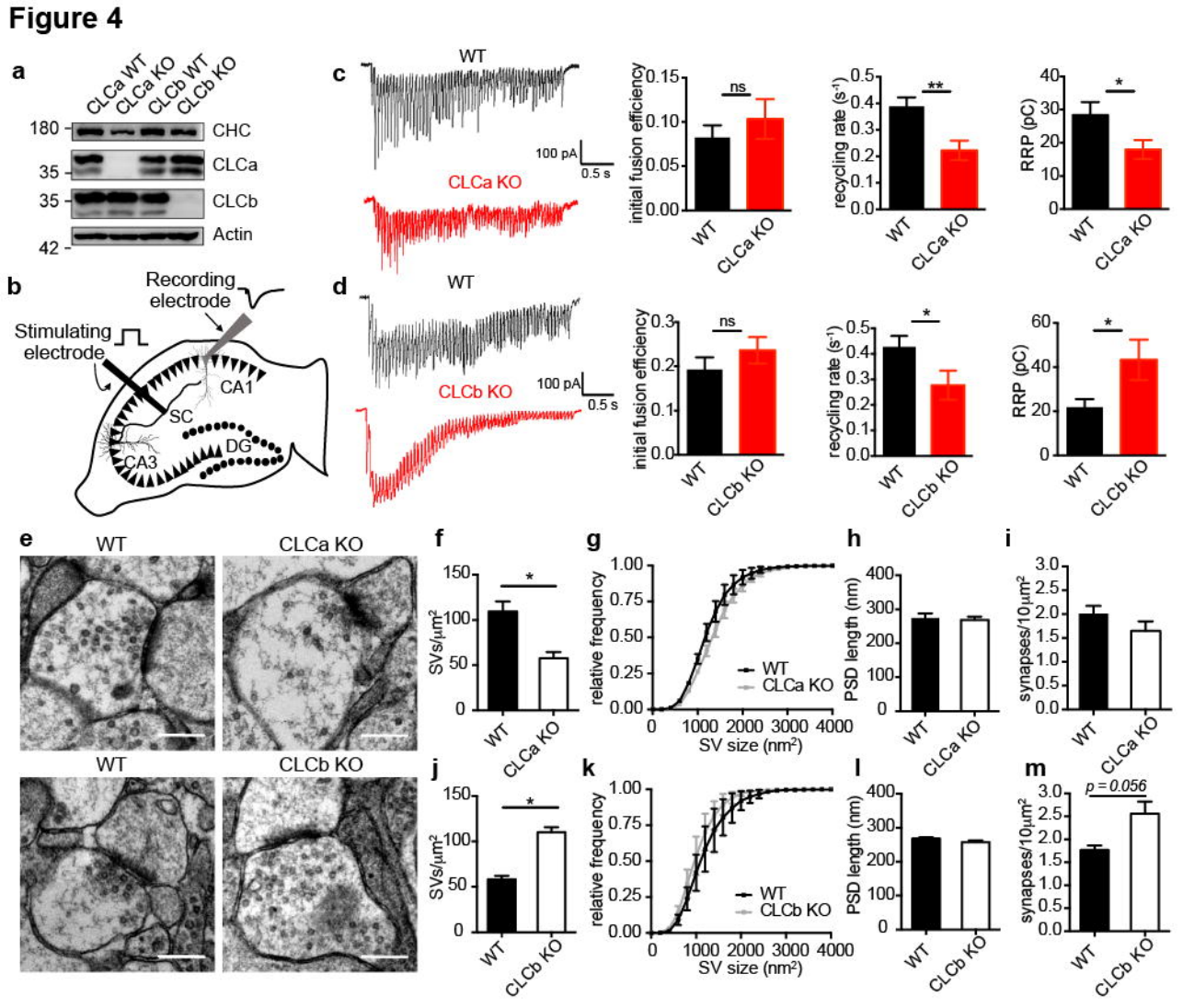
a
CLCa WT
CLCa KO
CLCb WT
CLCb KO
180
CHC
35
CLCa
35
CLCb
42
Actin
b
Recording electrode
Stimulating electrode
CA1
SC
DG
CA3
c
WT
100 pA
0.5 s
CLCa KO
initial fusion efficiency
ns
recycling rate (s-1)
**
RRP (pC)
*
d
WT
100 pA
0.5 s
CLCb KO
initial fusion efficiency
ns
recycling rate (s-1)
*
RRP (pC)
*
e
WT
CLCa KO
WT
CLCb KO
f
SVs/µm2
*
g
relative frequency
WT
CLCa KO
SV size (nm2)
h
PSD length (nm)
i
synapses/10µm2
j
SVs/µm2
*
k
relative frequency
WT
CLCb KO
SV size (nm2)
l
PSD length (nm)
m
synapses/10µm2
p = 0.056

Figure 5

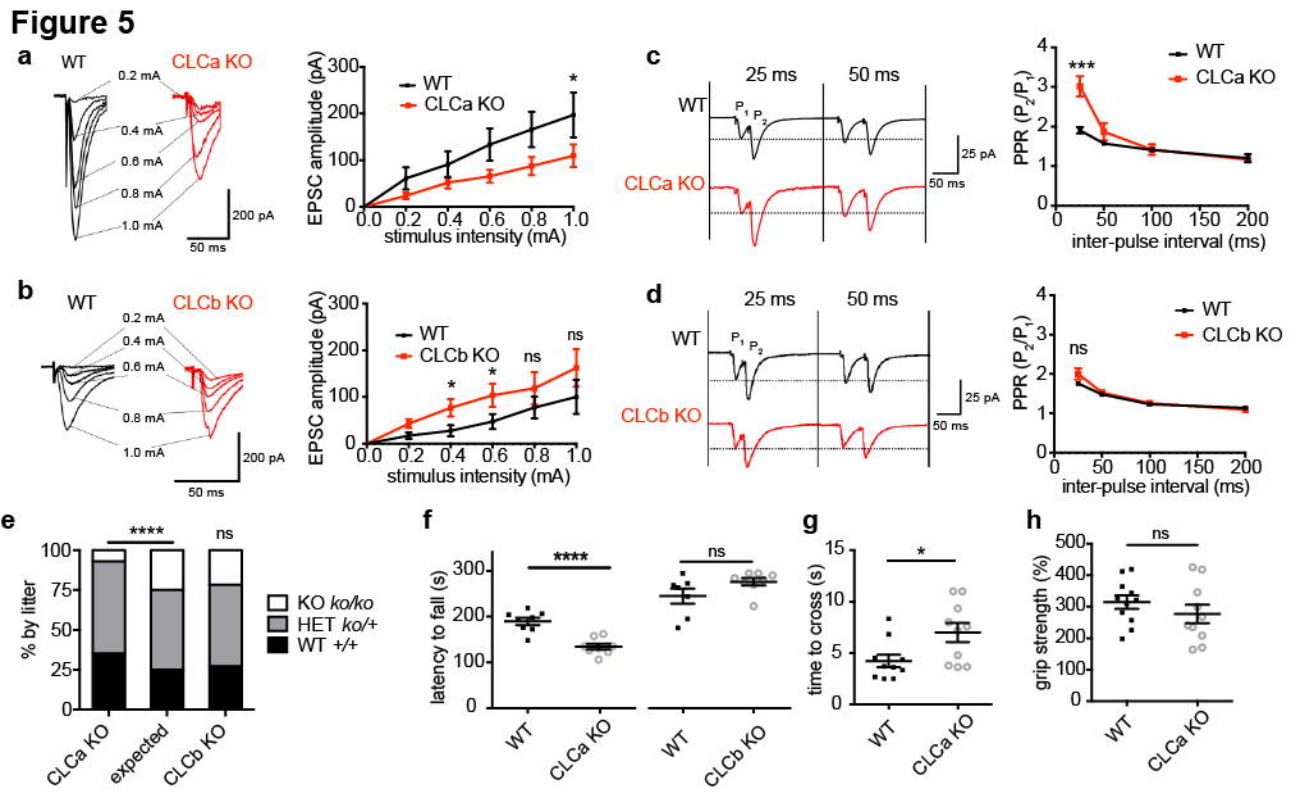
a
WT
CLCa KO
0.2 mA
0.4 mA
0.6 mA
0.8 mA
1.0 mA
200 pA
50 ms
EPSC amplitude (pA)
stimulus intensity (mA)
WT
CLCa KO
*
b
WT
CLCb KO
0.2 mA
0.4 mA
0.6 mA
0.8 mA
1.0 mA
200 pA
50 ms
EPSC amplitude (pA)
stimulus intensity (mA)
WT
CLCb KO
ns
*
*
ns
c
25 ms
50 ms
WT
CLCa KO
P1 P2
25 pA
50 ms
PPR (P2/P1)
inter-pulse interval (ms)
***
WT
CLCa KO
d
25 ms
50 ms
WT
CLCb KO
P1 P2
25 pA
50 ms
PPR (P2/P1)
inter-pulse interval (ms)
ns
WT
CLCb KO
e
****
ns
% by litter
KO ko/ko
HET ko/+
WT +/+
CLCa KO
expected
CLCb KO
f
****
ns
latency to fall (s)
WT
CLCa KO
WT
CLCb KO
g
*
time to cross (s)
WT
CLCa KO
h
ns
grip strength (%)
WT
CLCa KO

Figure 6

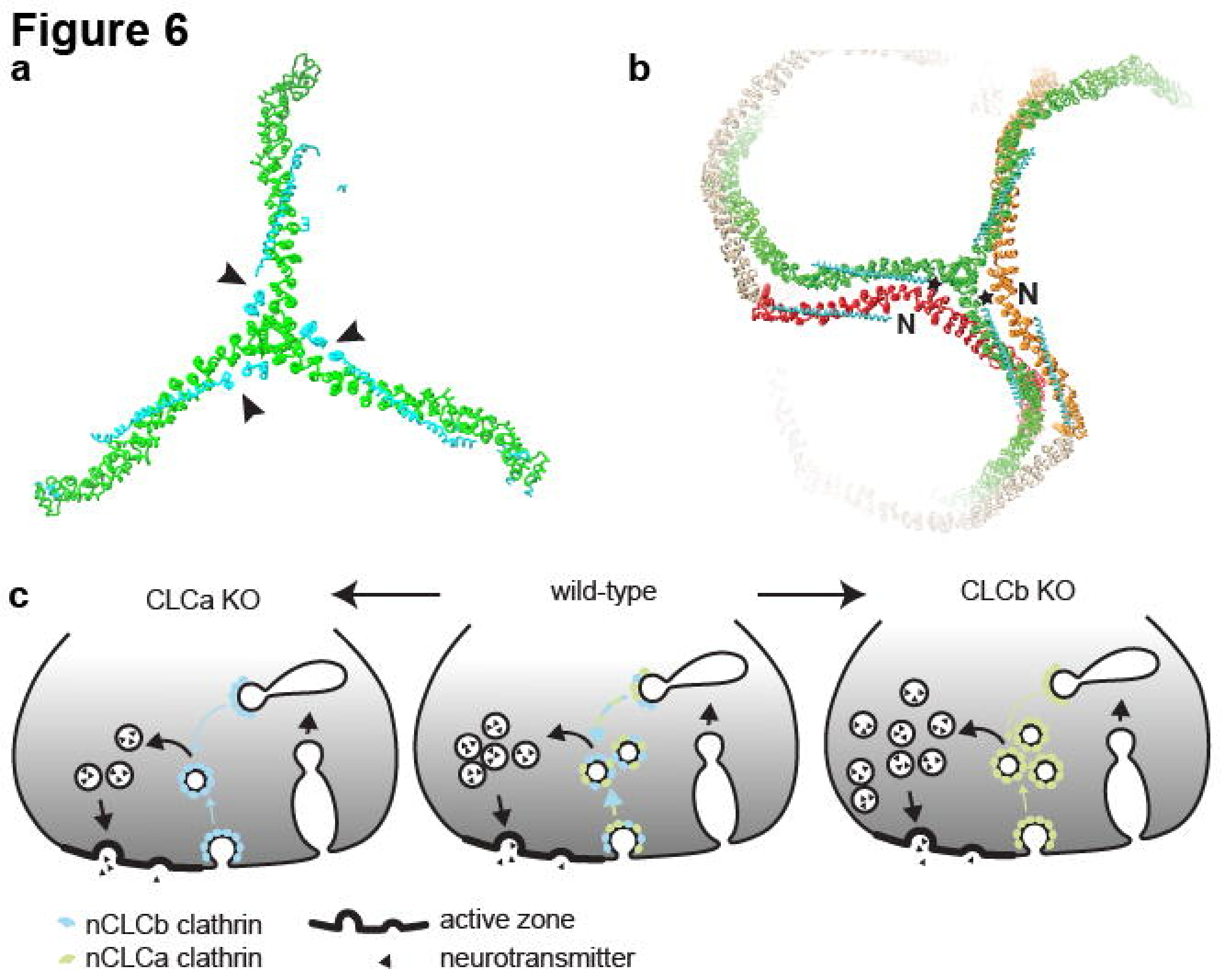
a
b
N
N
c
CLCa KO
wild-type
CLCb KO
nCLCb clathrin
nCLCa clathrin
active zone
neurotransmitter